


Non-Abelian Topological Phases and Their Quotient Relations in Acoustic Systems

Xiao-Chen Sun,^{1,2,‡} Jia-Bao Wang,^{1,‡} Cheng He,^{1,2,3,*} and Yan-Feng Chen^{1,2,3,†}

¹*National Laboratory of Solid State Microstructures and Department of Materials Science and Engineering, Nanjing University, Nanjing 210093, China*

²*Collaborative Innovation Center of Advanced Microstructures, Nanjing University, Nanjing 210093, China*

³*Jiangsu Key Laboratory of Artificial Functional Materials, Nanjing University, Nanjing 210093, China*

 (Received 8 May 2023; accepted 9 April 2024; published 24 May 2024)

Non-Abelian topological phases (NATPs) exhibit enigmatic intrinsic physics distinct from well-established Abelian topological phases, while lacking straightforward configuration and manipulation, especially for classical waves. In this Letter, we exploit novel braiding-type couplings among a pair of triple-component acoustic dipoles, which act as functional elements with effective imaginary couplings. Sequencing them in one dimension allows us to generate acoustic NATPs in a compact yet time-reversal invariant Hermitian system. We further provide the whole phase diagram that encompasses all i , j , and k non-Abelian phases, and directly demonstrate their unique quotient relations via different end point states. Our NATPs based on real-space braiding may inspire the exploration of acoustic devices with non-commutative characters.

DOI: [10.1103/PhysRevLett.132.216602](https://doi.org/10.1103/PhysRevLett.132.216602)

Topological phases (TPs) represent a novel form of matter [1–5] that has generated significant interest over the last decade for designing band topology in artificial materials, such as photonic and phononic crystals [6–18]. Their global behavior in the wave vector space (\mathbf{k} space) introduces robustness into energy bands, resulting in stable wave transmission against unavoidable perturbations in practical fabrications. The construction or breaking of nodal points or lines of two neighboring bands typically plays an essential role. One well-known case is topological semimetals with topological charges (TCs) attached to nodal points, which can manifest nontrivial Fermi arcs [19,20]. It is intriguing to consider TCs as attributes associated with the \mathbf{k} sphere or \mathbf{k} loop encompassing a nodal point in the Brillouin zone (BZ) [21–23]. Breaking such local band degeneracy further can give rise to topological insulators, whose topological invariants such as Chern number [1], Z_2 invariant [24], and Zak phase [25] characterize the global property of isolated bulk bands. Then, nontrivial boundary states appear in the band gap. So far, they have usually been used to deal with one gap or nodal points between two adjacent bands, most of which belong to the Abelian group with commutative property. For example, TCs with opposite values annihilate, creating gaps, while the same-valued TCs accumulate, transitioning linear degeneracy to quadratic. Further gapping such a quadratic degeneracy can lead to a system with a large Chern number [26].

Things could be very different with more than one band gap that can interact with each other. For instance, in a three-band system, there are two interactive band gaps and three kinds of possible degeneracies for every two bands,

corresponding to at least three kinds of TCs. They can “braid” with each other, which is a unique noncommutative operation intrinsically different from annihilation and accumulation. Two-dimensional (2D), three-dimensional (3D), and synthetic multiple dimensional topological semimetals or complex eigenvalue space in non-Hermitian systems are commonly considered to create sufficient dimensions for band braiding and non-Abelian topological charges (NATCs) [22,27–36]. Conversely, few studies have explored one-dimensional (1D) NA band topology due to the constrained degree of freedom in this dimension, which in practice necessitates additional parameter space and deliberate design, e.g., introducing imaginary couplings [23].

Although difficult to be realized, 1D NA systems have their own advantages compared to semimetals. One stems from their 1D BZ with periodic boundary conditions, that can be seen as a subset \mathbf{k} -loop surrounding some nodal points in a parent 2D space. Consequently, the 1D NA cases naturally upgrade to global NATPs, that can host end point states in the full band gaps, leading to more straightforward experimental observation. The other comes from their simple model, compact size, and hassle-free manipulation for future applications. A recent pioneering work demonstrated 1D NA electric circuit systems, which take advantage of its accessible complicated configurations by taking a subspace with both time-reversal (\mathcal{T}) and parity (\mathcal{P}) symmetries broken while the combined \mathcal{PT} symmetry is kept Hamiltonian [23]. But the \mathcal{T} -broken condition is not easy for spinless airborne sound and even particularly difficult [10] for possible complicated structures for braiding. For example, although the 2D acoustic quantum Hall effect based on \mathcal{T} -broken models [13,14,37] is one of the earliest

predicted acoustic topological phenomena, the experimental realization is scarce so far [38].

In this Letter, we report on the experimental implementation of NATPs in a 1D \mathcal{T} -invariant acoustic system. To achieve this, we incorporate an additional partner unit cell with braiding-type connecting tubes, which enables our acoustic system to realize positive, negative, and complex couplings within a single model. As a result, we observe all i , j , and k phases belonging to the NA quaternion group \mathbb{Q} , featuring end point states and the generation of a phase diagram. Furthermore, we verify quotient relations between different NATPs. Based on the 1D \mathcal{T} -invariant acoustic system, our NATP paves a compact way to explore non-commutative devices for classical waves.

Guaranteed by \mathcal{PT} symmetry, the eigenvectors of the system are pure real under a specific basis, which makes the normalized vector matrix of a complete three-band gapped system belonging to the orthogonal group $O(3)$. Because a vector can only be determined up to a sign \pm , the order-parameter space of the Hamiltonian is the space $M_3 = O(3)/O(1)^3$. Degeneracies of bands invalidate the discussion above and play as the obstacle of a S^1 loop in M_3 , which can be exactly described by the fundamental group π_1 . In our case, $\pi_1(M_3) = \mathbb{Q} = \{+1, \pm i, \pm j, \pm k, -1\}$, the NA quaternion group as shown in Fig. 1(a) [22,23]. It comprises three anticommuting imaginary units that satisfy $ij = -ji = k$, $jk = -kj = i$, $ki = -ik = j$, and $i^2 = j^2 = k^2 = -1$, showing the invalid of the commutative law. Physically, $+1$ represents the trivial topology while $\{\pm i\}$, $\{\pm j\}$, $\{\pm k\}$, and $\{-1\}$ represent different NATCs. A physical interpretation of this group is visualized in Fig. 1(b), where two nodal points in a 2D three-band system represent degeneracies between the 2nd & 3rd and 1st & 2nd bands, respectively. Because of the symmetry, the wave vectors are pure real and acquire an additional π phase along the k loop surrounding the nodal point, leading

to the assignment of charges $i(k)$. As the system evolves with some parameter P , nodal points move along a braiding trajectory and the k loop extends to a cylinder in the P -BZ space. Inside the k cylinder, nodal point on every intersecting surface indicates that NATC undergoes a process of $+k \sim 1 \sim +i \sim 1 \sim -k$. The sign of k changes due to the NA braiding $iki^{-1} = k^{-1} = -k$ [22], leading to the bouncing of nodal points [31–33] (see Fig. S1 in the Supplemental Material [39]). The only difference between the 1D and 2D cases is that 1D BZ itself forms a k loop and can be taken as a subspace in a 2D parent system. In this sense, a local NATC upgrades to a global NATP [yellow lines and arrow in Fig. 1(b)]. The intersection between the nodal point trajectory and the k cylinder indicates the phase transition points, where the band gaps close [Fig. 1(b)]. As dictated by the bulk-boundary correspondence, end point or interface state must exist at the boundary [Fig. 1(c)]. For example, a 1D system with $+k$ NATC shown in Fig. 1(b) has an end point between the 1st and 2nd bands as shown in the lower panel of Fig. 1(c).

One way to realize a theoretical model containing such NATCs requires different types of couplings, including positive, negative, and imaginary values [23], necessitating \mathcal{T} -broken condition. It has been established that positive and negative couplings can be achieved by connecting cavities in the opposite and same directions, respectively, by utilizing acoustic dipole modes because the in-phase eigenvalue is larger or smaller than the out-of-phase eigenvalue [40–42]. The expansion of the realm of coupling coefficients leads to the higher-order topological insulators and projection symmetry-protected Mobius topological states, showcasing a profound new theory and phenomenon [43]. Very recently, it has been confirmed that positive and negative couplings introduce the twisted π -flux block and, equivalently, a pair of \mathcal{T} -invariant complex hopping [44] (see Fig. S3 [39]). For practical

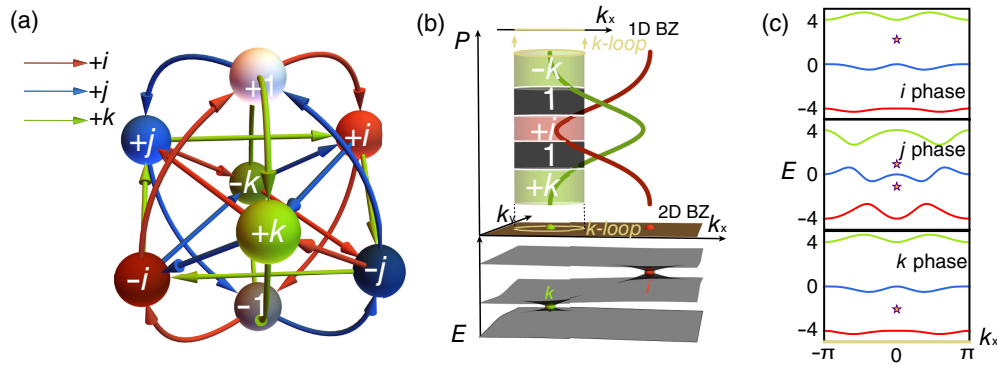


FIG. 1. NATCs in bands. (a) Quaternion group. Balls represent group elements, and conjugate elements are in a similar color. For example, $\pm i$ are in light and dark red, respectively, while they are in the same topological class. Arrows in red, blue, and green define mutual multiplications by $+i$, $+j$, and $+k$, respectively. For example, $(+i) \cdot (\text{blue } \rightarrow) = (+k)$. (b) Schematic of the NATCs. DPs i and k project onto the 2D BZ on a brown plane, marked as red and green dots, respectively. A k -loop circling DP- k in the origin changes its NATCs with P increasing. A 1D BZ can be taken as such a loop in a high-dimensional space. (c) Band structure of i , j , and k phases. Different phases feature different end point states.

implementation, we use a braiding type of coupling tubes to ensure uniform length among all the tubes, and the coupling strength is controlled by diameters. Additionally, we reshape the cavities into a U shape, which enables tuning of on-site energy by their length and minimizes the difference between the acoustic model and the tight-binding approach (TBA) [45].

One unit cell contains 6 acoustic cavities, taking advantage of braiding-type couplings conveniently constructed via dipoles in U-shaped cavities. There are 3 cavities in one layer for the requirement of 3 bands, and a set of partners on the other layer for the construction of conjugate imaginary couplings, as shown in Fig. 2(a), with sublattice index X_α ($X = A, B, C$), $\alpha = \uparrow, \downarrow$, respectively. The corresponding TBA model is shown in Fig. 2(b). Their on-site energies are marked as $S_{X_\uparrow} = S_{X_\downarrow} \equiv S_X$, which is controlled by the length of the cavity h_X . There are no inner cell couplings between these 6 cavities. The intercell couplings can be expressed as $v_{(X_\alpha, n), (Y_\beta, n+1)} [\delta(X, Y) - \delta(\alpha, \beta) = 0]$, indicating that only couplings with exact the same or totally different index exist. We further constrain that $v_{(X_\uparrow, n), (X_\uparrow, n+1)} = v_{(X_\downarrow, n), (X_\downarrow, n+1)} \equiv v_X$ and $v_{(X_\downarrow, n), (Y_\uparrow, n+1)} = -v_{(X_\uparrow, n), (Y_\downarrow, n+1)} = v_{(Y_\downarrow, n), (X_\uparrow, n+1)} = -v_{(Y_\uparrow, n), (X_\downarrow, n+1)} \equiv v_{XY}$, with n marks the unit cell. All connecting tubes have the same length, and the strength of coupling is determined by their diameter d_X/d_{XY} . In practice, we use the sign “ $\pm d$ ” to

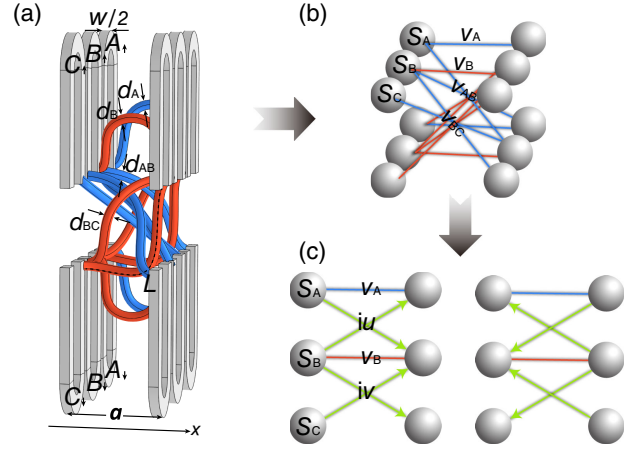


FIG. 2. Model construction. (a) Two layers of acoustic structure. U-shaped cavities are connected with effective positive couplings by red tubes, and negative couplings by blue tubes. All the tubes share the same length $L = 7$ cm. The lattice constant is $a = 3$ cm, and the width of the cavity is $W = 0.48$ cm. Other parameters are shown in Table I [39]. (b) TBA model with pure real couplings. (c) Effective TBA model with imaginary couplings.

indicate positive or negative couplings and mark them as red or blue in Fig. 2(a). The TBA Hamiltonian in a 1D chain can be constructed (see details in [39]) and further expanded in k_x space as

$$\begin{aligned}
 H(k_x) &= \begin{bmatrix} H_d(k_x) & iH_o(k_x) \\ -iH_o(k_x) & H_d(k_x) \end{bmatrix} \\
 H_d(k_x) &= \begin{bmatrix} S_A + 2v_A \cos k_x & 0 & 0 \\ 0 & S_B + 2v_B \cos k_x & 0 \\ 0 & 0 & S_C + 2v_C \cos k_x \end{bmatrix} \\
 H_o(k_x) &= 2 \sin k_x \begin{bmatrix} 0 & v_{AB} & v_{CA} \\ v_{AB} & 0 & v_{BC} \\ v_{CA} & v_{BC} & 0 \end{bmatrix}, \quad (1)
 \end{aligned}$$

with the basis $(A_\uparrow, B_\uparrow, C_\uparrow, A_\downarrow, B_\downarrow, C_\downarrow)$. With the unitary transformation $U = \exp(i\tau_x \otimes \sigma_0 \pi/4)$, in which τ_x is the x component of Pauli matrix and σ_0 is the 3×3 identical matrix, the Hamiltonian can be diagonalized with new basis $(A_\uparrow + iA_\downarrow, B_\uparrow + iB_\downarrow, C_\uparrow + iC_\downarrow, A_\uparrow - iA_\downarrow, B_\uparrow - iB_\downarrow, C_\uparrow - iC_\downarrow)/\sqrt{2}$:

$$\begin{aligned}
 H_0(k_x) &= UH(k_x)U^\dagger \\
 &= \begin{bmatrix} H_d(k_x) + H_o(k_x) & 0 \\ 0 & H_d(k_x) - H_o(k_x) \end{bmatrix} \\
 &\equiv \begin{bmatrix} H_+(k_x) & 0 \\ 0 & H_-(k_x) \end{bmatrix}. \quad (2)
 \end{aligned}$$

$H_\pm(k_x)$ are Hamiltonian with a pair of \mathcal{T} -symmetric conjugate NATCs. The effective model is shown in Fig. 2(c).

In contrast to the Berry phase usually used to characterize topology of sole one bandgap, the topological property of the current two related band gaps can be described by the NA charge:

$$Q = \overline{\exp} \left[\oint A(k_x) \cdot dk_x \right] \quad (3)$$

where $A(k_x) = \sum_t \beta_t [-(i/2)\sigma_t]$ with σ_t as the Pauli Matrix, $\beta_t = \sum_{pq} \langle u^p | \partial_{k_x} | u^q \rangle \epsilon_{tpq} / 2$ calculated from bands p and q , ϵ_{tpq} being fully antisymmetric tensor. The bar over the

exponent indicates path ordering. The results of quaternion group elements are represented as Pauli matrix $1 \rightarrow \sigma_0$, $i \rightarrow i\sigma_x$, $j \rightarrow i\sigma_y$, and $k \rightarrow i\sigma_z$, where σ_0 is the 2 X 2 identity matrix. It should be noticed that the signs \pm only have relative meaning for NATCs i, j , and k , but distinguish the trivial phase 1 and nontrivial phase -1 for the unit 1. $\pm i(\pm j, \pm k)$ can only be distinguished up to a basepoint, which means that a pair of conjugate charges cannot be distinguished by observing them separately. Their difference only manifests as interface states sandwiched by them [23]. In this sense, although our design cannot distinguish a pair of conjugate NATCs, it provides a good platform to study one single phase and the interface between phases in different classes. In the following, we use the NATC of $H_+(k_x)$ to represent a specific system.

The 9 parameters in H_+ can be classified into 3 groups: 3 on-site energies $S_{A,B,C}$, 3 intercell couplings with the same letter index v_X , and 3 intercell couplings with different letter index v_{XY} . The first two groups are in the diagonal position of the Hamiltonian. The sum of each group ($S_A + S_B + S_C$ & $v_A + v_B + v_C$) does not affect the NATC, because they can only shift or scale the bands. To ensure orthogonality, we set the other parameters

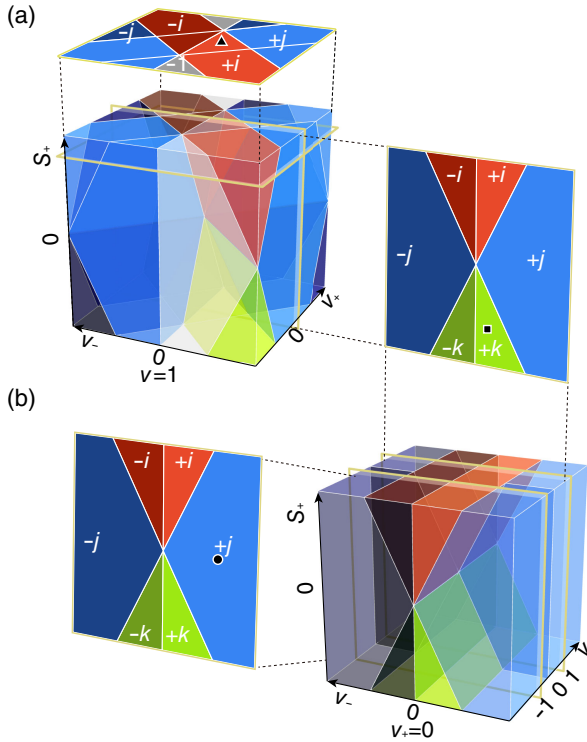


FIG. 3. NATP diagram. (a) NATP diagram spanned by parameters v_{\pm} and S_{\pm} . $\pm i, \pm j, \pm k$, and -1 phases are in red, blue, green, and gray, respectively. Slices of $S_{\pm} = 12$ and $v_{\pm} = 0$ are picked to mark representative states i and k by triangle and square, respectively. (b) Phase diagram spanned by parameters v , v_{-} , and S_{\pm} . Its $v = 1$ slice is just the $v_{+} = 0$ in (a). Slice $v = -1$ is selected to mark representative state j by a circle.

as $S_A - S_B \equiv S_{-}$, $S_A + S_B - 2S_C \equiv S_{+}$, $v_A - v_B \equiv v_{-}$, $v_A + v_B - 2v_C \equiv v_{+}$, $v_{AB} \equiv u$, $v_{BC} \equiv v$, and $v_{CA} \equiv w$. Without the loss of generality, we neglect the long-range coupling ($w = 0$) and the difference of the first two sites ($S_{-} = 0$), and set $u = 1$ as the unit. We obtain a phase diagram with 3 of remaining parameters: v_{-} , v_{+} and S_{+} as shown in Fig. 3(a) leaving $v = 1$ (see Fig. S4 [39]).

1D NATPs feature end point states in bulk gaps. We first select states in i and k phases marked as triangle and square, respectively, in Fig. 3(a) (Details of parameters can be found in Table I [39]). The sample of phase i with probe and source is presented in Fig. 4(a) (see Fig. S5 [39]). All samples are fabricated using photosensitive resin via 3D printing, regarded as an acoustic hard boundary. We drill some round holes on the cavities at the upper and lower surfaces and print a corresponding plug for the convenience of measurements. In the frequency range we focus on, there are three bands with two gaps. Nontrivial NATPs can be clarified by the rotation of the state when wave vector k_x goes through the loop $-\pi/a$ to π/a . For instance, in the i phase, the states of the 2nd and 3rd bands get π phase while the lowest state maintains its sign (see Fig. S6 [39]). If we embed the 1D BZ into a parent 2D BZ by replacing $\cos k_x$ and $\sin k_y$ with k_x and k_y , a degeneracy between 2nd and 3rd bands can be found. Consequently, we can see an end point state between the twisting bands. The experiment results are shown in Fig. 4(b), which agree with the simulation and TBA results (see Fig. S7 [39]). Simulations are implemented by the commercial software COMSOL Multiphysics based on a finite element method. The states in the k phase twist its

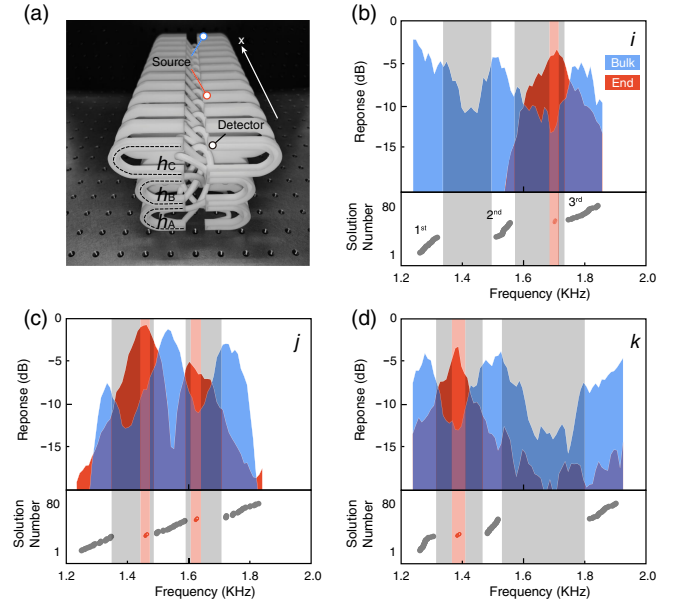


FIG. 4. End point states of a single phase. (a) A sample of phase i and the experimental setup to detect the response. Parameters are shown in Table I [39]. (b)–(d) Responses of phases i , j , and k , respectively. Simulated solutions are shown in the lower panel.

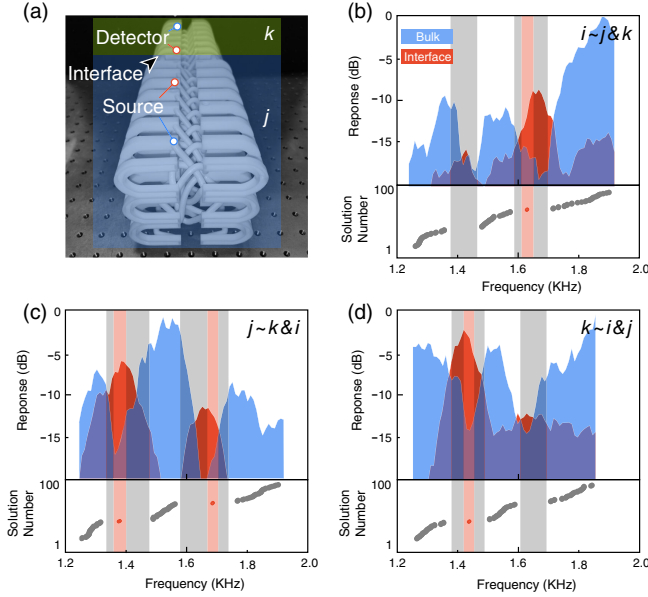


FIG. 5. Interface states between different phases. (a) A sample of phase j vs k and the experimental setup to detect the response. Parameters are shown in Table I [39]. (b)–(d) Responses of interfaces j vs k , k vs i , and i vs j , respectively. Simulated solutions are shown in the lower panel.

1st and 2nd bands and manifest an end point state between them as shown in Fig. 4(d).

The phase diagram provides us with more information when the fourth dimension is introduced. By fixing $v_+ = 0$, and treating inactive v as an axis, we obtain the phase diagram in Fig. 3(b). It is worth noting that the slice of $v = 1$ in Fig. 3(b) is identical to the slice $v_+ = 0$ in Fig. 3(a). The phases appear to be unaffected along the v axis, except for the band degeneracy at $v = 0$, which does not lead to a phase transition. We select a state in the j phase denoted by a circle, which twist its 1st and 3rd bands, and two sets of states sandwich the 2nd band and can be observed [Fig. 4(c)]. Another phase diagram is shown in Fig. S8 [39], which shows the tunable nature of our system.

In the Abelian case, such as Berry phase in Chern insulators, the domain-wall act as the difference of two phases sandwiching it: $\Delta Q = Q_L - Q_R$, which transitions to quotient relations in NA scenario: $\Delta Q = Q_L Q_R^{-1} = Q_L / Q_R$ [23]. Specifically, the domain-wall between phases j & k (k & i , i & j) acts similarly the end point in one single phase $i(j, k)$. In fact, both Abelian and NA cases follow the same rule that the domain-wall state is determined by the original and inverse value of topological invariants on its two sides, respectively. The experimental sample with the detector and source marked is shown in Fig. 5(a). NA quotient relations are visible in our acoustic systems, as shown in Figs. 5(b)–5(d).

In summary, our Letter demonstrates the realization of NATPs in the \mathcal{T} -invariant acoustic system. In a similar way, a more compact \mathcal{T} -broken model based on air-flow

background [14] with a minimum three-atom unit cell, could be used to realize analogous NATPs (see Fig. S9 in [39]). Through this temporal modulation, the nonreciprocal even nonlinear non-Abelian braiding process could be explored in the future, which might be relevant to the impact of phonon dynamics on coherence or other quantum mechanical phenomena [46]. The concept of NATP can be further combined with non-Hermitian [29] and Floquet topology [47], or other NA braiding processes [48–52] to explore new phenomena. In contrast to its 2D and 3D counterparts, 1D NA topology exhibits a distinct end point state in a complete gap, making it a promising candidate for designing functional primitive structures. By utilizing acoustic dipole modes, we effectively implement positive, negative, and equivalently complex couplings, making acoustic crystals a versatile platform for simulating almost all kinds of TBA models in theory. Our design only requires one auxiliary unit cell and provides probably the simplest method to achieve effective complex couplings in practice, which could be useful for compact devices. The model could be realized in a finite size sample, preserving the essence of NA physics (see Fig. S10 [39]). The connecting tubes can be replaced by soft tubes, making it a plug-and-play and tunable topological device designs. The phase diagrams obtained with different parameters reveal the system's distinct physical properties, directly indicating the topological intricacy and can potentially provide a clear and definitive roadmap for future NA topological device development.

The work was jointly supported by the National Key R&D Programme of China [Grant No. 2022YFA1404302 (C. H.)] and the National Natural Science Foundation of China [Grants No. 52022038 (C. H.), No. 92263207 (C. H.), No. 11874196 (C. H.), No. 11890700 (Y.-F. C.), No. 51721001 (Y.-F. C.), No. 52027803 (Y.-F. C.), and No. 52103341 (X.-C. S.)].

X.-C. S. and C. H. conceived the original idea. X.-C. S. performed the theoretical portions of this work. J.-B. W. conducted the experiments. C. H. and Y.-F. C. supervised the project. All authors contributed to the analyses and the preparation of the Letter.

*Corresponding author: chenghe@nju.edu.cn

†Corresponding author: yfchen@nju.edu.cn

‡X.-C. S. and J.-B. W. contributed equally to this work.

- [1] D. J. Thouless, M. Kohmoto, M. P. Nightingale, and M. den Nijs, Quantized Hall conductance in a two-dimensional periodic potential, *Phys. Rev. Lett.* **49**, 405 (1982).
- [2] B. A. Bernevig, T. L. Hughes, and S.-C. Zhang, Quantum spin Hall effect and topological phase transition in HgTe quantum wells, *Science* **314**, 1757 (2006).
- [3] M. König, S. Wiedmann, C. Brüne, A. Roth, H. Buhmann, L. W. Molenkamp, X.-L. Qi, and S.-C. Zhang, Quantum

- spin Hall insulator state in HgTe quantum wells, *Science* **318**, 766 (2007).
- [4] B. A. Bernevig and S.-C. Zhang, Quantum spin Hall effect, *Phys. Rev. Lett.* **96**, 106802 (2006).
- [5] C. L. Kane and E. J. Mele, Quantum spin Hall effect in graphene, *Phys. Rev. Lett.* **95**, 226801 (2005).
- [6] Z. Wang, Y. Chong, J. D. Joannopoulos, and M. Soljačić, Observation of unidirectional backscattering-immune topological electromagnetic states, *Nature (London)* **461**, 772 (2009).
- [7] A. B. Khanikaev, S. Hossein Mousavi, W.-K. Tse, M. Kargarian, A. H. MacDonald, and G. Shvets, Photonic topological insulators, *Nat. Mater.* **12**, 233 (2013).
- [8] M. C. Rechtsman, J. M. Zeuner, Y. Plotnik, Y. Lumer, D. Podolsky, F. Dreisow, S. Nolte, M. Segev, and A. Szameit, Photonic Floquet topological insulators, *Nature (London)* **496**, 196 (2013).
- [9] M. Hafezi, S. Mittal, J. Fan, A. Migdall, and J. M. Taylor, Imaging topological edge states in silicon photonics, *Nat. Photonics* **7**, 1001 (2013).
- [10] R. Fleury, D. L. Sounas, C. F. Sieck, M. R. Haberman, and A. Alù, Sound isolation and giant linear nonreciprocity in a compact acoustic circulator, *Science* **343**, 516 (2014).
- [11] M. Xiao, G. Ma, Z. Yang, P. Sheng, Z. Q. Zhang, and C. T. Chan, Geometric phase and band inversion in periodic acoustic systems, *Nat. Phys.* **11**, 240 (2015).
- [12] L.-H. Wu and X. Hu, Scheme for achieving a topological photonic crystal by using dielectric material, *Phys. Rev. Lett.* **114**, 223901 (2015).
- [13] A. B. Khanikaev, R. Fleury, S. H. Mousavi, and A. Alù, Topologically robust sound propagation in an angular-momentum-biased graphene-like resonator lattice, *Nat. Commun.* **6**, 8260 (2015).
- [14] Z. Yang, F. Gao, X. Shi, X. Lin, Z. Gao, Y. Chong, and B. Zhang, Topological acoustics, *Phys. Rev. Lett.* **114**, 114301 (2015).
- [15] X. Cheng, C. Jouvaud, X. Ni, S. H. Mousavi, A. Z. Genack, and A. B. Khanikaev, Robust reconfigurable electromagnetic pathways within a photonic topological insulator, *Nat. Mater.* **15**, 542 (2016).
- [16] C. He, X. Ni, H. Ge, X.-C. Sun, Y.-B. Chen, M.-H. Lu, X.-P. Liu, and Y.-F. Chen, Acoustic topological insulator and robust one-way sound transport, *Nat. Phys.* **12**, 1124 (2016).
- [17] X. Ni, M. A. Gorlach, A. Alu, and A. B. Khanikaev, Topological edge states in acoustic kagome lattices, *New J. Phys.* **19**, 055002 (2017).
- [18] G. Ma, M. Xiao, and C. T. Chan, Topological phases in acoustic and mechanical systems, *Nat. Rev. Phys.* **1**, 281 (2019).
- [19] X. Wan, A. M. Turner, A. Vishwanath, and S. Y. Savrasov, Topological semimetal and Fermi-arc surface states in the electronic structure of pyrochlore iridates, *Phys. Rev. B* **83**, 205101 (2011).
- [20] L. Lu, L. Fu, J. D. Joannopoulos, and M. Soljačić, Weyl points and line nodes in gyroid photonic crystals, *Nat. Photonics* **7**, 294 (2013).
- [21] C. Fang, H. Weng, X. Dai, and Z. Fang, Topological nodal line semimetals, *Chin. Phys. B* **25**, 117106 (2016).
- [22] Q. Wu, A. A. Soluyanov, and T. Bzdušek, Non-Abelian band topology in noninteracting metals, *Science* **365**, 1273 (2019).
- [23] Q. Guo, T. Jiang, R.-Y. Zhang, L. Zhang, Z.-Q. Zhang, B. Yang, S. Zhang, and C. T. Chan, Experimental observation of non-Abelian topological charges and edge states, *Nature (London)* **594**, 195 (2021).
- [24] C. L. Kane and E. J. Mele, Z₂ topological order and the quantum spin Hall effect, *Phys. Rev. Lett.* **95**, 146802 (2005).
- [25] P. Delplace, D. Ullmo, and G. Montambaux, Zak phase and the existence of edge states in graphene, *Phys. Rev. B* **84**, 195452 (2011).
- [26] S. A. Skirlo, L. Lu, and M. Soljačić, Multimode one-way waveguides of large Chern numbers, *Phys. Rev. Lett.* **113**, 113904 (2014).
- [27] M. Wang, S. Liu, Q. Ma, R.-Y. Zhang, D. Wang, Q. Guo, B. Yang, M. Ke, Z. Liu, and C. T. Chan, Experimental observation of non-Abelian earring nodal links in phononic crystals, *Phys. Rev. Lett.* **128**, 246601 (2022).
- [28] Y. S. S. Patil, J. Höller, P. A. Henry, C. Guria, Y. Zhang, L. Jiang, N. Kralj, N. Read, and J. G. E. Harris, Measuring the knot of non-Hermitian degeneracies and non-commuting braids, *Nature (London)* **607**, 271 (2022).
- [29] K. Wang, A. Dutt, C. C. Wojcik, and S. Fan, Topological complex-energy braiding of non-Hermitian bands, *Nature (London)* **598**, 59 (2021).
- [30] Q. Zhang, Y. Li, H. Sun, X. Liu, L. Zhao, X. Feng, X. Fan, and C. Qiu, Observation of acoustic non-Hermitian Bloch braids and associated topological phase transitions, *Phys. Rev. Lett.* **130**, 017201 (2023).
- [31] A. Bouhon, Q. Wu, R.-J. Slager, H. Weng, O. V. Yazyev, and T. Bzdušek, Non-Abelian reciprocal braiding of Weyl points and its manifestation in ZrTe, *Nat. Phys.* **16**, 1137 (2020).
- [32] B. Jiang, A. Bouhon, Z.-K. Lin, X. Zhou, B. Hou, F. Li, R.-J. Slager, and J.-H. Jiang, Experimental observation of non-Abelian topological acoustic semimetals and their phase transitions, *Nat. Phys.* **17**, 1239 (2021).
- [33] H. Qiu, Q. Zhang, T. Liu, X. Fan, F. Zhang, and C. Qiu, Minimal non-Abelian nodal braiding in ideal metamaterials, *Nat. Commun.* **14**, 1261 (2023).
- [34] D. Cheng, K. Wang, and S. Fan, Artificial non-Abelian lattice gauge fields for photons in the synthetic frequency dimension, *Phys. Rev. Lett.* **130**, 083601 (2023).
- [35] D. Wang, B. Yang, M. Wang, R.-Y. Zhang, X. Li, Z. Q. Zhang, S. Zhang, and C. T. Chan, Observation of non-Abelian charged nodes linking nonadjacent gaps, *Phys. Rev. Lett.* **129**, 263604 (2022).
- [36] M. Ezawa, Non-Hermitian non-Abelian topological insulators with PT symmetry, *Phys. Rev. Res.* **3**, 043006 (2021).
- [37] X. Ni, C. He, X.-C. Sun, X. Liu, M.-H. Lu, L. Feng, and Y.-F. Chen, Topologically protected one-way edge mode in networks of acoustic resonators with circulating air flow, *New J. Phys.* **17**, 053016 (2015).
- [38] Y. Ding, Y. Peng, Y. Zhu, X. Fan, J. Yang, B. Liang, X. Zhu, X. Wan, and J. Cheng, Experimental demonstration of acoustic Chern insulators, *Phys. Rev. Lett.* **122**, 014302 (2019).

- [39] See Supplemental Material at <http://link.aps.org/supplemental/10.1103/PhysRevLett.132.216602> for a theoretical description of non-Abelian topological charges and model constructions, as well as some experimental details and results.
- [40] X. Ni, M. Li, M. Weiner, A. Alù, and A. B. Khanikaev, Demonstration of a quantized acoustic octupole topological insulator, *Nat. Commun.* **11**, 2108 (2020).
- [41] H. Xue, Y. Ge, H.-X. Sun, Q. Wang, D. Jia, Y.-J. Guan, S.-Q. Yuan, Y. Chong, and B. Zhang, Observation of an acoustic octupole topological insulator, *Nat. Commun.* **11**, 2442 (2020).
- [42] Y. Qi, C. Qiu, M. Xiao, H. He, M. Ke, and Z. Liu, Acoustic realization of quadrupole topological insulators, *Phys. Rev. Lett.* **124**, 206601 (2020).
- [43] Y. X. Zhao, Y.-X. Huang, and S. A. Yang, Z_2 -projective translational symmetry protected topological phases, *Phys. Rev. B* **102**, 161117(R) (2020).
- [44] L. Shao, Z. Chen, K. Wang, S. A. Yang, and Y. Zhao, Spinless mirror Chern insulator from projective symmetry algebra, *Phys. Rev. B* **108**, 205126 (2023).
- [45] Z.-G. Chen, L. Wang, G. Zhang, and G. Ma, Chiral symmetry breaking of tight-binding models in coupled acoustic-cavity systems, *Phys. Rev. Appl.* **14**, 024023 (2020).
- [46] C. Nayak, S. H. Simon, A. Stern, M. Freedman, and S. Das Sarma, Non-Abelian anyons and topological quantum computation, *Rev. Mod. Phys.* **80**, 1083 (2008).
- [47] R.-J. Slager, A. Bouhon, and F. N. Ünal, Floquet multi-gap topology: Non-Abelian braiding and anomalous Dirac string phase, *Nat. Commun.* **15**, 1144 (2024).
- [48] Y.-K. Sun, X.-L. Zhang, F. Yu, Z.-N. Tian, Q.-D. Chen, and H.-B. Sun, Non-Abelian Thouless pumping in photonic waveguides, *Nat. Phys.* **18**, 1080 (2022).
- [49] Z.-G. Chen, R.-Y. Zhang, C. T. Chan, and G. Ma, Classical non-Abelian braiding of acoustic modes, *Nat. Phys.* **18**, 179 (2022).
- [50] X.-L. Zhang, F. Yu, Z.-G. Chen, Z.-N. Tian, Q.-D. Chen, H.-B. Sun, and G. Ma, Non-Abelian braiding on photonic chips, *Nat. Photonics* **16**, 390 (2022).
- [51] O. You, S. Liang, B. Xie, W. Gao, W. Ye, J. Zhu, and S. Zhang, Observation of non-Abelian Thouless pump, *Phys. Rev. Lett.* **128**, 244302 (2022).
- [52] Y. Yang, C. Peng, D. Zhu, H. Buljan, J. D. Joannopoulos, B. Zhen, and M. Soljačić, Synthesis and observation of non-Abelian gauge fields in real space, *Science* **365**, 1021 (2019).